OPTIMAL MEASUREMENT CONFIGURATION IN COMPUTATIONAL DIFFRACTIVE IMAGING

Evan Widloski *Ulas Kamaci* *Farzad Kamalabadi*

Department of Electrical and Computer Engineering and Coordinated Science Laboratory,
University of Illinois at Urbana-Champaign, Urbana, IL 61801, USA

ABSTRACT

Diffractive lenses have recently been applied to the domain of multispectral imaging in the X-ray and UV regimes where they can achieve very high resolution as compared to reflective and refractive optics. Conventionally, spectral components are reconstructed by taking measurements at the focal planes. However, the reconstruction quality can be improved by optimizing the measurement configuration. In this work, we adapt a sequential backward selection algorithm to search for a configuration which minimizes expected reconstruction error. By approximating the forward system as a circular convolution and making assumptions on the source and noise, we greatly reduce the complexity of the algorithm. Numerical results show that the configuration found by the algorithm significantly improves the reconstruction performance compared to a standard configuration.

***Index Terms*—** Spectral imaging, diffractive optics, measurement configuration, subset selection, computational imaging

1. INTRODUCTION

Spectral imaging is the formation of images at different wavelengths in the electromagnetic spectrum. With images usually taken in the visible, X-ray, ultraviolet (UV), or infrared bands, it has applications in medicine, geographic surveying, astronomy, and solar physics [1], [2]. In spectral imaging, a polychromatic source must be first separated into its spectral components before being captured. There are a number of ways to achieve this, but a common method is to use a set of configurable optical filters. For example, the spectral imager on the Solar Dynamics Observatory uses a rotating drum of optical filters to selectively pass light of specific wavelengths of interest [3].

A new approach is to use a diffractive lens to perform spectral imaging [4]. Diffractive lenses are often preferred in the UV or X-ray regimes because manufacturing tolerances at these wavelengths can be more relaxed than reflective optics and still obtain a similar resolution [5]. Since diffractive optics can be manufactured using a photolithographic process, they can be produced at a higher precision compared to the grinding process used to produce conventional reflective optics. Moreover, refractive optics are unsuitable for UV or X-ray imaging because glass is opaque at these wavelengths. Figures 1(b) and 1(c) are two examples of a pattern that can be etched into silicon wafer to produce a diffractive lens.

Diffractive lenses have the property that the angle at which light exits the lens is determined by the light's wavelength, which gives them a wavelength dependent focal length, as shown in Figure 1(a) [6].

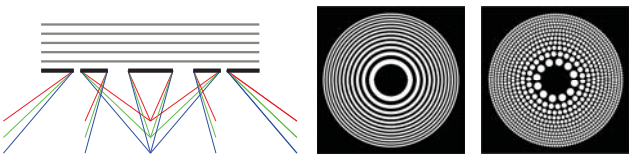

Fig. 1. (a) diffraction of a polychromatic wave through a diffractive lens (b) Fresnel zone plate (c) photon sieve [7]

Measurements at the focal plane of each spectral component comprise of a sum of a focused image of one component and blurred images of all other components, as shown in Figure 2. An inverse problem consisting of disentangling and deblurring of measurements must be solved in order to recover the original source components [4]. However, this focal plane measurement configuration leads to suboptimal reconstructions, especially when spectral components are close in wavelength. Therefore, it is desired to determine the optimal measurement configuration before acquiring the data.

Finding the optimal measurement configuration can be seen as a *sensor placement problem*, which lies under the broader class of problems known as *subset selection*. Subset selection applies to many domains, such as array optimization for atmospheric imaging [8], [9], magnetic resonance imaging [10], and detection problems [11]. Methods like genetic algorithms, convex optimization [12], and hill climbing [13] with many selection criteria have been developed to solve such problems.

However, most of these methods solve the problem of single-sensor/single-measurement systems where the placement of one sensor contributes a single row to the observa-

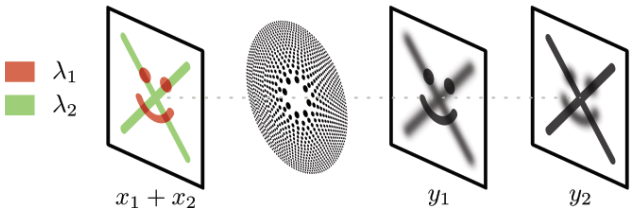

Fig. 2. Imaging a scene with emissions at wavelengths λ_1 and λ_2. Measurements y_1 and y_2 are taken at two positions where one wavelength is in focus and the other is out of focus.

tion matrix. In contrast, many imaging systems are single-sensor/multiple-measurement (like our problem), where each sensor placed (measurement plane) contributes multiple rows to the observation matrix (one row per detector pixel). Single-sensor/single-measurement algorithms have been extended to the multiple measurement case, known as *clustering* algorithms. Examples include *clustered sequential backward selection* (CSBS) [8], *clustered FrameSense* (CFS) [14], *clustered maximum projection on minimum eigenspace* (CMPME) [15].

In this paper we adapt CSBS to the diffractive imaging problem to automatically determine a measurement configuration from a set of candidate plane locations, which minimizes expected reconstruction error. Furthermore, we exploit structures in the imaging model to make the algorithm computationally feasible for large images.

2. FORWARD MODEL AND STATISTICAL FORMULATION

In this section, we mathematically model a diffractive imaging system and describe the process of recovering the spectral components. Consider a polychromatic source that has S spectral components $\boldsymbol{x}_1, \ldots, \boldsymbol{x}_S \in \mathbb{R}^{N_1 \times N_1}$. Using a moving detector, we make M measurements $\boldsymbol{y}_1, \ldots, \boldsymbol{y}_M \in \mathbb{R}^{N_2 \times N_2}$ at distances $d_1, \ldots, d_M$ from the lens. We allow for repeated measurements at the same plane for a more flexible model that can take into account non equal exposure times. Due to linearity, each measurement is a superposition of blurred versions of the S sources. More formally,

$$\boldsymbol{y}_m = \sum_{s=1}^{S} \boldsymbol{a}_{m,s} * \boldsymbol{x}_s + \boldsymbol{n}_m \tag{1}$$

where $\boldsymbol{a}_{m,s} \in \mathbb{R}^{P \times P}$ is a blurring kernel known as a *point spread function* (PSF), $*$ is a 2D convolution, and $\boldsymbol{n}_m \in \mathbb{R}^{N_2 \times N_2}$ is additive measurement noise. Each PSF depends on the associated source wavelength and measurement location together with the diffractive lens parameters and can be computed efficiently [16].

Since convolution is a linear operation, we can rewrite the above equation as a linear system

$$\underbrace{\begin{bmatrix} \boldsymbol{y}_1 \\ \vdots \\ \boldsymbol{y}_M \end{bmatrix}}_{\boldsymbol{y}} = \underbrace{\begin{bmatrix} \boldsymbol{A}_{1,1} & \ldots & \boldsymbol{A}_{1,S} \\ \vdots & & \vdots \\ \boldsymbol{A}_{M,1} & \ldots & \boldsymbol{A}_{M,S} \end{bmatrix}}_{\boldsymbol{A_d}} \underbrace{\begin{bmatrix} \boldsymbol{x}_1 \\ \vdots \\ \boldsymbol{x}_S \end{bmatrix}}_{\boldsymbol{x}} + \underbrace{\begin{bmatrix} \boldsymbol{n}_1 \\ \vdots \\ \boldsymbol{n}_M \end{bmatrix}}_{\boldsymbol{n}} \tag{2}$$

where $\boldsymbol{y}_m \in \mathbb{R}^{N_2^2 \times 1}$, $\boldsymbol{x}_s \in \mathbb{R}^{N_1^2 \times 1}$ and $\boldsymbol{n}_m \in \mathbb{R}^{N_2^2 \times 1}$ have been flattened from their original 2D shape, and each $\boldsymbol{A}_{m,s} \in \mathbb{R}^{N_2^2 \times N_1^2}$ is a block-toeplitz matrix with toeplitz blocks formed from 2D convolution with PSF $\boldsymbol{a}_{m,s}$. We will refer to the matrix containing all $\boldsymbol{A}_{m,s}$ generated by measurements taken at $\boldsymbol{d} = \{d_1, \ldots, d_M\}$ as $\boldsymbol{A_d}$.

The problem of where to take measurements $\boldsymbol{y}_1, \ldots, \boldsymbol{y}_M$ has not been addressed and affects the reconstruction quality. In order to compare the impact of different measurement configurations on the reconstruction, it is necessary to define some cost for the measurement matrix $\boldsymbol{A_d}$. A common cost metric is the expected reconstruction error, or expected *sum of squared errors* (SSE). However, we must have some strategy for the recovery of $\boldsymbol{x}$ to get reconstruction error and we must make statistical assumptions about $\boldsymbol{x}$. *Maximum a posteriori* (MAP) estimation is one such strategy.

We assume the original spectral components and noise are distributed according to a normal distribution such that $\boldsymbol{x} \sim \mathcal{N}(\boldsymbol{x}_0, \boldsymbol{\Sigma_x})$ and $\boldsymbol{n} \sim \mathcal{N}(0, \boldsymbol{\Sigma_n})$. The MAP estimate is then

$$\begin{aligned} \boldsymbol{x}_{MAP} &= \arg\max_{\boldsymbol{x} \in \mathbb{C}^n} p(\boldsymbol{x}|\boldsymbol{y}) = \arg\max_{\boldsymbol{x}} p(\boldsymbol{y}|\boldsymbol{x}) p(\boldsymbol{x}) \\ &= \arg\min_{\boldsymbol{x}} \left[-\log(p(\boldsymbol{y}|\boldsymbol{x})) - \log p(\boldsymbol{x}) \right] \\ &= \boldsymbol{x}_0 + \left(\boldsymbol{A_d}^H \boldsymbol{\Sigma_n}^{-1} \boldsymbol{A_d} + \boldsymbol{\Sigma_x}^{-1} \right)^{-1} \cdot \boldsymbol{A_d}^H \boldsymbol{\Sigma_n}^{-1} (\boldsymbol{y} - \boldsymbol{A_d} \boldsymbol{x}_0) \end{aligned}$$

The reconstruction error is defined as $\boldsymbol{e} = \boldsymbol{x} - \boldsymbol{x}_{\text{MAP}}$, and the expected sum of squared error cost is $E[\|\boldsymbol{e}\|_2^2]$. This expression can be rewritten in terms of the error covariance:

$$\begin{aligned} \mathbb{E}[\|\boldsymbol{e}\|_2^2] = \mathbb{E}[\boldsymbol{e}^H \boldsymbol{e}] = \mathbb{E}[\text{tr}(\boldsymbol{e}^H \boldsymbol{e})] = \mathbb{E}[\text{tr}(\boldsymbol{e}\boldsymbol{e}^H)] \\ = \text{tr}(\mathbb{E}[\boldsymbol{e}\boldsymbol{e}^H]) = \text{tr}(\boldsymbol{\Sigma_e}) \end{aligned}$$

where the error covariance matrix is defined as $\boldsymbol{\Sigma_e} = E[\boldsymbol{e}\boldsymbol{e}^H]$ and has the closed form expression:

$$\boldsymbol{\Sigma_e} = \left(\boldsymbol{A_d}^H \boldsymbol{\Sigma_n}^{-1} \boldsymbol{A_d} + \boldsymbol{\Sigma_x}^{-1} \right)^{-1} \tag{3}$$

Combining the above equations, we can now write a cost metric which lets us evalute the expected reconstruction error for a particular measurement configuration $\boldsymbol{d}$:

$$\text{Cost}(\boldsymbol{d}) = \mathbb{E}[\|\boldsymbol{e}\|_2^2] = \text{tr}\left(\left(\boldsymbol{A_d}^H \boldsymbol{\Sigma_n}^{-1} \boldsymbol{A_d} + \boldsymbol{\Sigma_x}^{-1} \right)^{-1} \right) \tag{4}$$

3. MEASUREMENT SELECTION ALGORITHM

With a method of evaluating the effect a particular configuration $\boldsymbol{d}$ has on reconstruction error, we can begin considering which configurations are best suited for minimizing error. For example, if we are provided with a set of C candidate measurement locations, we may wish to find a subset of size M which minimizes reconstruction error. This is known as a *subset selection* problem. One might think to simply search over all possible measurement configurations of size M, but this exhaustive search requires $\binom{C}{M}$ evalutions of cost, growing on the order of $O(C^M)$.

CSBS is an alternative method which is more computationally feasible, where one measurement location is eliminated from $\boldsymbol{d}$ in each iteration until only M locations remain. As reconstruction error generally increases as the number of measurements decreases, CSBS selects for elimination the measurement that incurs the smallest increase in cost in each iteration.

Algorithm 1 CSBS Algorithm

$\boldsymbol{d} = \{d_1, \ldots, d_C\}$
repeat
  $d' = \arg\min_{d \in \boldsymbol{d}} \text{Cost}(\boldsymbol{d} \backslash \{d\}))$
  $\boldsymbol{d} = \boldsymbol{d} \backslash \{d'\}$
until $|\boldsymbol{d}| = M$

Unlike an exhaustive search, the complexity of CSBS is not combinatorial. As the size of $\boldsymbol{d}$ shrinks with each iteration, the number of cost evaluations for each minimization step decreases. The total number of cost evaluations is

$$\sum_{|\boldsymbol{d}|=M}^{C} |\boldsymbol{d}| = O(C^2 - M^2)$$

4. FAST IMPLEMENTATION

While the SSE cost applies to any general linear system, we can augment the complexity reduction achieved by CSBS by making assumptions about the structure of $\boldsymbol{A_d}$, $\boldsymbol{\Sigma_n}$ and $\boldsymbol{\Sigma_x}$. Specifically, if we assume the blocks of these matrices are block-circulant with circulant blocks (BCCB), then they can be diagonalized by the 2D DFT matrix where operations involving multiplications and inversions are much faster.

For $\boldsymbol{A_d}$ this means that each block $\boldsymbol{A}_{m,s}$ is BCCB and corresponds to circular convolution with the kernel $\boldsymbol{a}_{m,s}$. For $\boldsymbol{\Sigma}_n$, we assume independent noise among image pixels and measurement planes with variance $(1/\lambda)$, so $\boldsymbol{\Sigma}_n = (1/\lambda)\boldsymbol{I}$ where $\boldsymbol{I}$ represents the identity matrix. For $\boldsymbol{\Sigma}_x$, each of its blocks being BCCB means that the covariance among image pixels are represented by 2D convolution kernels.

Assuming $N \times N$ images, each $N^2 \times N^2$ block $\boldsymbol{A}_{m,s}$ of $\boldsymbol{A_d}$ can be decomposed as $\boldsymbol{A}_{m,s} = \boldsymbol{F}^{-1}\widetilde{\boldsymbol{A}}_{m,s}\boldsymbol{F}$ where $\widetilde{\boldsymbol{A}}_{m,s}$ is the diagonal matrix consisting of the 2D DFT of $\boldsymbol{a}_{m,s}$, and $\boldsymbol{F}$ is the 2D DFT matrix. This yields

$$\boldsymbol{A_d} = \underbrace{\begin{bmatrix} \boldsymbol{F}^{-1} & & 0 \\ & \ddots & \\ 0 & & \boldsymbol{F}^{-1} \end{bmatrix}}_{\widetilde{\boldsymbol{F}}^{-1}} \underbrace{\begin{bmatrix} \widetilde{\boldsymbol{A}}_{1,1} & \ldots & \widetilde{\boldsymbol{A}}_{1,S} \\ \vdots & \ddots & \vdots \\ \widetilde{\boldsymbol{A}}_{M,1} & \ldots & \widetilde{\boldsymbol{A}}_{M,S} \end{bmatrix}}_{\widetilde{\boldsymbol{A}}_{\boldsymbol{d}}} \underbrace{\begin{bmatrix} \boldsymbol{F} & & 0 \\ & \ddots & \\ 0 & & \boldsymbol{F} \end{bmatrix}}_{\widetilde{\boldsymbol{F}}} \quad (5)$$

so, we have $\boldsymbol{A_d} = \widetilde{\boldsymbol{F}}^{-1}\widetilde{\boldsymbol{A}}_{\boldsymbol{d}}\widetilde{\boldsymbol{F}}$, from which we get $\boldsymbol{A_d}^H\boldsymbol{A_d} = \widetilde{\boldsymbol{F}}^{-1}\widetilde{\boldsymbol{A}}_{\boldsymbol{d}}^H\widetilde{\boldsymbol{A}}_{\boldsymbol{d}}\widetilde{\boldsymbol{F}}$. Applying the same procedure, we get $\boldsymbol{\Sigma}_x^{-1} = \widetilde{\boldsymbol{F}}^{-1}\widetilde{\boldsymbol{\Sigma}}_x^{-1}\widetilde{\boldsymbol{F}}$. The SSE cost for a measurement configuration $\boldsymbol{d}$ then becomes (scaling both terms with λ):

$$\begin{aligned} \text{Cost}(\boldsymbol{d}) &= \text{tr}\left(\left(\boldsymbol{A_d}^H\boldsymbol{A_d} + \lambda\boldsymbol{\Sigma}_x^{-1}\right)^{-1}\right) \quad (6) \\ &= \text{tr}\left(\left(\widetilde{\boldsymbol{F}}^{-1}\left(\widetilde{\boldsymbol{A}}_{\boldsymbol{d}}^H\widetilde{\boldsymbol{A}}_{\boldsymbol{d}} + \lambda\widetilde{\boldsymbol{\Sigma}}_x^{-1}\right)\widetilde{\boldsymbol{F}}\right)^{-1}\right) \\ &= \text{tr}\left(\widetilde{\boldsymbol{F}}^{-1}\left(\widetilde{\boldsymbol{A}}_{\boldsymbol{d}}^H\widetilde{\boldsymbol{A}}_{\boldsymbol{d}} + \lambda\widetilde{\boldsymbol{\Sigma}}_x^{-1}\right)^{-1}\widetilde{\boldsymbol{F}}\right) \\ &= \text{tr}\left(\left(\widetilde{\boldsymbol{A}}_{\boldsymbol{d}}^H\widetilde{\boldsymbol{A}}_{\boldsymbol{d}} + \lambda\widetilde{\boldsymbol{\Sigma}}_x^{-1}\right)^{-1}\right) \quad (7) \end{aligned}$$

where the computational complexity of evaluating (7) is much less than (6) due to the diagonalized blocks of $\widetilde{\boldsymbol{A}}_{\boldsymbol{d}}$ and $\widetilde{\boldsymbol{\Sigma}}_x^{-1}$.

There are two contributors to the complexity of evaluating the cost at $\text{Cost}(\boldsymbol{d})$ for a particular configuration: The multiplication $\widetilde{\boldsymbol{A}}_{\boldsymbol{d}}^H\widetilde{\boldsymbol{A}}_{\boldsymbol{d}}$, and the inversion $\left(\widetilde{\boldsymbol{A}}_{\boldsymbol{d}}^H\widetilde{\boldsymbol{A}}_{\boldsymbol{d}} + \lambda\widetilde{\boldsymbol{\Sigma}}_x^{-1}\right)^{-1}$. In fact, the product $\widetilde{\boldsymbol{A}}_{\boldsymbol{d}}^H\widetilde{\boldsymbol{A}}_{\boldsymbol{d}}$ only needs to be calculated once during the algorithm initialization, and it can be efficiently updated at each iteration by adding/subracting the contribution of the candidate plane that is iterated over, which can be precomputed.

Thus, the complexity of overall CSBS algorithm is dominated by the inversion of $\left(\widetilde{\boldsymbol{A}}_{\boldsymbol{d}}^H\widetilde{\boldsymbol{A}}_{\boldsymbol{d}} + \lambda\widetilde{\boldsymbol{\Sigma}}_x^{-1}\right) \in \mathbb{C}^{SN^2 \times SN^2}$ that is performed in each iteration. While the complexity of a standard inversion algorithm is $O((SN^2)^3)$, the diagonal structure of this matrix allows for a much faster inversion algorithm with complexity $O(S^3N^2)$, a speed-up of N^4 which is significant for large images.

The total CSBS algorithm complexity is

$$O_{sbs} = \sum_{|\boldsymbol{d}|=M}^{C} |\boldsymbol{d}| O(S^3N^2) = O(S^3N^2C^2)$$

5. NUMERICAL EXPERIMENTS

In this section, we present numerical experiments that demonstrate that the measurement configuration selected by CSBS yields improved reconstructions over reconstructions obtained from measurements taken at focal planes. We use a photon sieve as the diffractive element in our simulations, which offers PSFs with sharper focus than Fresnel zone plates [7].

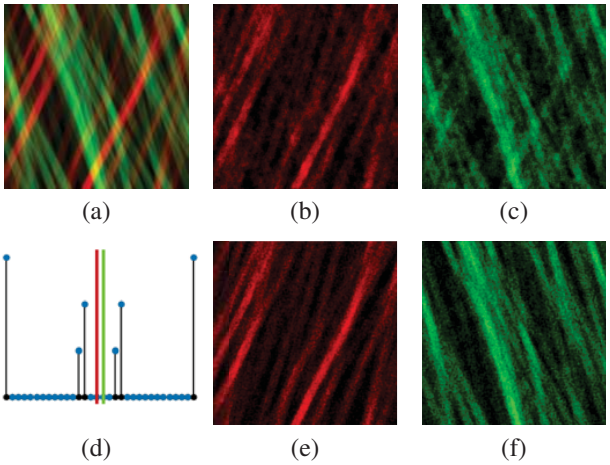

Fig. 3. (a) polychromatic source image with spectral components λ_1 and λ_2 (b) reconstruction of λ_1 from focal configuration (c) reconstruction of λ_2 from focal configuration (d) measurement locations selected by CSBS (e) reconstruction of λ_1 from CSBS configuration (f) reconstruction of λ_2 from CSBS configuration

We begin by simulating a scenario with two spectral components that are close to each other in wavelength, shown as separate colors in Figure 3(a). We use the MAP estimation framework given in Section 2 as the image reconstruction algorithm for both the focal plane and CSBS configurations. For a fair comparison between CSBS and focal plane reconstructions, we search over λ to find the value which maximizes the focal plane reconstruction *structural similarity* (SSIM) [17], then use this same λ for the CSBS cost function and reconstruction. The final measurement configuration selected by CSBS is given in Figure 3(d), where the two focal planes are marked with red and green bars. Figures 3(b) and 3(c) show the spectral component reconstructions for the focal plane configuration, and Figures 3(e) and 3(f) for CSBS configuration. The reconstruction SSIMs for the CSBS and focal plane reconstructions are 0.459 and 0.347, respectively.

Our intuition on why CSBS chooses out of focus planes pertains to measurement variation of the PSF pairs for each candidate plane. The spectral components are very close together in wavelength, so the PSFs corresponding to in focus and out of focus components at the focal planes are very similar. This leads to poor measurement variation and makes disentangling the component contributions difficult. This is especially evident in Figure 3(c), where the features from one wavelength appear in the reconstruction of the other wavelength. Instead, CSBS chooses measurement locations where the PSF pairs have more variation at the expense of a less sharp in focus PSF, shown in Figure 4.

To show that this reconstruction improvement generalizes, we repeat the first experiment for $S = 2, 3, 4$ uniformly spaced spectral components under different noise levels and

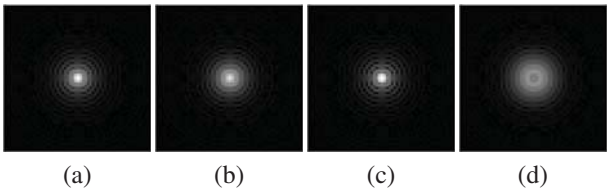

Fig. 4. (a) (b) PSFs at λ_1 focal plane. (c) (d) PSFs at a measurement location selected by CSBS (c) and (d) are less focused that (a) and (b), but have more measurement variation between them.

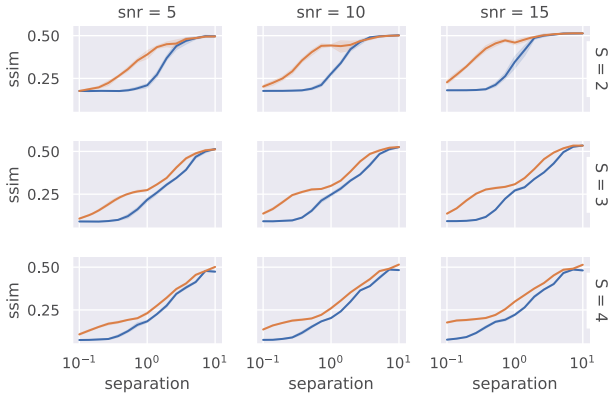

Fig. 5. Reconstruction SSIMs for varied number of spectral components, SNR (dB), and source separation (DOF). CSBS reconstruction SSIM and focal plane reconstruction SSIM are shown in orange and blue, respectively.

spectral component separations measured in depth of focus (DOF) [5]. In Figure 5, we plot the mean SSIM of the reconstructions obtained from measurements at focal planes (blue) and measurements at planes selected by CSBS (orange). The CSBS reconstructions generally have higher SSIM than the focal plane up until the spectral components are sufficiently separated (about 10 DOF), where reconstruction SSIM are about the same.

6. CONCLUSION

We apply a variant of the sequential backward selection algorithm to the problem of acquisition in a diffractive spectral imaging system. The high dimensionality of large images makes a direct application of CSBS and SSE cost computationally intractable, so we have developed a more feasible implementation of this algorithm and perform an analysis of its complexity to show that it is significantly faster than the previous implementation for large images. Finally, we demonstrate CSBS on a simulated spectral imaging system and show that the optimized measurement configuration achieves equal or better reconstructions than a choice of measurements at the spectral component focal planes.

7. REFERENCES

[1] G. A. Shaw and H. K. Burke, "Spectral imaging for remote sensing," *Lincoln laboratory journal*, vol. 14, no. 1, pp. 3–28, 2003.

[2] Y. Garini, I. T. Young, and G. McNamara, "Spectral imaging: principles and applications," *Cytometry Part A: The Journal of the International Society for Analytical Cytology*, vol. 69, no. 8, pp. 735–747, 2006.

[3] J. R. Lemen, D. J. Akin, P. F. Boerner, C. Chou, J. F. Drake, D. W. Duncan, C. G. Edwards, F. M. Friedlaender, G. F. Heyman, N. E. Hurlburt, et al., "The atmospheric imaging assembly (aia) on the solar dynamics observatory (sdo)," in *The solar dynamics observatory*, pp. 17–40. Springer, 2011.

[4] F. S. Oktem, F. Kamalabadi, and J. M. Davila, "High-resolution computational spectral imaging with photon sieves," in *2014 IEEE International Conference on Image Processing (ICIP)*. IEEE, 2014, pp. 5122–5126.

[5] J. M. Davila, "High-resolution solar imaging with a photon sieve," in *Solar Physics and Space Weather Instrumentation IV*. International Society for Optics and Photonics, 2011, vol. 8148, p. 81480O.

[6] D. Attwood, *Soft X-rays and extreme ultraviolet radiation: principles and applications*, Cambridge university press, 1999.

[7] L. Kipp, M. Skibowski, R. Johnson, R. Berndt, R. Adelung, S. Harm, and R. Seemann, "Sharper images by focusing soft x-rays with photon sieves," *Nature*, vol. 414, no. 6860, pp. 184–188, 2001.

[8] B. Sharif and F. Kamalabadi, "Optimal sensor array configuration in remote image formation," *IEEE Transactions on Image Processing*, vol. 17, 2008.

[9] J. Wang and A. Yarovoy, "Near-optimal selection of gpr observations for linear inversion," in *Proc. 9th Int. Workshop Adv. Ground Penetrating Radar*, 2017, pp. 1–5.

[10] Y. Gao and S. J. Reeves, "Optimal k-space sampling in mrsi for images with a limited region of support," *IEEE transactions on medical imaging*, vol. 19, no. 12, pp. 1168–1178, 2000.

[11] C.-T. Yu and P. K. Varshney, "Sampling design for gaussian detection problems," *IEEE transactions on signal processing*, vol. 45, no. 9, pp. 2328–2337, 1997.

[12] S. Joshi and S. Boyd, "Sensor selection via convex optimization," *IEEE Transactions on Signal Processing*, vol. 57, no. 2, pp. 451–462, 2008.

[13] S. J. Reeves and Z. Zhe, "Sequential algorithms for observation selection," *IEEE Transactions on Signal Processing*, vol. 47, no. 1, pp. 123–132, 1999.

[14] J. Ranieri, A. Chebira, and M. Vetterli, "Near-optimal sensor placement for linear inverse problems," *IEEE Transactions on signal processing*, vol. 62, no. 5, pp. 1135–1146, 2014.

[15] J. Wang and A. Yarovoy, "Sampling design of synthetic volume arrays for three-dimensional microwave imaging," *IEEE Transactions on Computational Imaging*, vol. 4, no. 4, pp. 648–660, 2018.

[16] S. Ayazgok and F. S. Oktem, "Efficient computation of 2d point-spread functions for diffractive lenses," *Applied Optics*, vol. 59, no. 2, pp. 445–451, 2020.

[17] Zhou Wang, A. C. Bovik, H. R. Sheikh, and E. P. Simoncelli, "Image quality assessment: from error visibility to structural similarity," *IEEE Transactions on Image Processing*, vol. 13, no. 4, pp. 600–612, April 2004.